

Descent and modification of the overflow plume in the Denmark Strait

James B. Girton and Thomas B. Sanford
Applied Physics Laboratory and Department of Oceanography
University of Washington

Abstract. We examine the bulk properties of the Denmark Strait Overflow plume derived from velocity and hydrography surveys undertaken in 1997 and 1998. Despite the presense of considerable short-term variability, we find that the pathway and evolution of the plume density anomaly are remarkably steady. Bottom stress measurements show that the pathway of the plume core matches well with a rate of descent controlled by friction. The estimated entrainment rate diagnosed from the rate of plume dilution is consistent with previous estimates from current meter array transports and shows a marked increase in entrainment after 125 km from the sill. This increase is likely due to increased topographic slopes in the region or due to decreasing Richardson number as the plume is diluted.

Introduction

Dense water from the deep convective regions of the North Atlantic produces a signature of the thermohaline overturning circulation that can be seen as far away as the Pacific and Indian oceans. The Denmark Strait is one of the most geographically-confined locations along this entire “conveyor belt” pathway, and so is a region of great importance to researchers interested in understanding the forcing and modifications of the overturning circulation by its individual components, as well as to those interested in monitoring the strength of the circulation on long timescales. In addition, physical processes such as entrainment and bottom drag occur in many similar density currents and overflows, so that knowledge obtained in one is applicable to others.

The ultimate properties of the deep water being formed are determined not only by the direct processes of air-sea interaction that create the initial overflowing water but also by the mixing with and entrainment of surrounding fluid during the density current’s descent. For this reason, the location and mechanism of entrainment is of vital

importance to the ability to simulate deep water changes in ocean models. This combination of localized small-scale physics and global importance presents a particularly difficult challenge for the large-scale numerical models used to study the ocean and global climate. Even with continual improvements in computational power, the resolution needed to simulate overflow processes will not be available on a global scale in the foreseeable future, and so a realistic approach to subgrid-scale parameterization (based on observations) is needed.

Past Observations of the DSO

Products The fate of the DSO and other Nordic Seas outflows has been studied extensively using hydrographic measurements throughout the North Atlantic during the 1950s through 1970s as summarized by *Swift* [1984]. Later measurements [*Smethie and Swift*, 1989; *Livingston et al.*, 1985] added a more comprehensive set of tracers to the mix, but definitive estimates of transport and the evolution of the overflows from violent sill flow to (more-or-less) steady boundary current were not available until the deployment of a set of moorings by the UK Lowestoft laboratories at 3 sites

along the southeast coast of Greenland [Dickson and Brown, 1994]. These moorings showed the increase in transport of the DSO from 3 to 5 Sv through entrainment during its initial descent as well as subsequent increases to 10 Sv due to the joining of the Iceland–Scotland overflows and eventually to 13 Sv at the southern tip of Greenland after gradual additional mixing.

A somewhat different picture of the overflows' effects is given by the consideration of the spreading rates of atmospheric tracers [Doney and Jenkins, 1994] and tracer inventories [Smethie and Fine, 2001]. While the direct pathways of boundary currents are clearly important, the spreading of tracers seems to give almost equal weight to lateral processes such as isopycnal stirring and mixing by eddies. The integrating effects of tracers is clearly useful in preventing aliasing by high-frequency variability, but does make conclusions about time-dependent effects difficult.

Another major contribution of the Lowestoft arrays was to reveal a lack of seasonal or interannual variability in the transport of the overflow waters. This led to an apparent contradiction, given the substantial changes in Greenland Sea convective activity throughout the year and from year to year. The contradiction has been partially explained by the more gradual transformation process described by Mauritzen [1996] but the question does remain as to what timescale of forcing the overflow will respond to. Recent efforts have focused on the possibility of connections between the Overflow and convective processes in the Nordic Seas, possibly related to decadal forcing by the North Atlantic Oscillation [McCartney *et al.*, 1998; Bacon, 1998; Dickson *et al.*, 1999]. Clearly, if the dramatic changes in deepwater formation suggested by the paleo records were to occur, the dense overflows should be one of the first places that the effects would be apparent.

Overflow The ICES “OVERFLOW ’73” expedition [described in Ross, 1984; Smith, 1976, and hereafter referred to as O73] was far more successful and has remained the most comprehensive set of mooring and hydrographic section data from the

Denmark Strait region until very recently. The 37-day long mooring deployment in O73 showed that the DSO is highly variable on timescales of 2–5 days but steady over longer periods, with a mean transport of 2.9 Sv of water colder than 2°C. Tides play only a small role in the variability, accounting for 2–10% of the variance in the current meter velocities. These data form a large part of the historical context for the new measurements presented in this dissertation. The year-long MONA array about 100 km downstream from the O73 location corroborated these conclusions and revealed a lack of variability on seasonal timescales [Aagaard and Malmberg, 1978].

Since 1993 the Nordic WOCE and EC-VEINS programs have undertaken a number of cruises to the Denmark Strait sill and nearby regions. Two of these cruises on the Finnish R/V *Aranda* are described by Fristedt *et al.* [1999] and Rudels *et al.* [1999]. In recent years the German government has also undertaken a number of cruises with the F/S *Poseidon* and other vessels to the region, some of which have been briefly described by Krauss and Käse [1998]. This paper describes results from velocity-profiling instruments deployed on two of the above-mentioned cruises on the *Aranda* and *Poseidon* in 1997 and 1998.

Surveys with expendables

Due to the combined effects of variability on short temporal and spatial scales, we chose to undertake a rapid, high-resolution survey of the Denmark Strait region using ship-lowered (CTD) and expendable (XCP, XCTD) profiling instruments to measure velocity, temperature and salinity. The expendable instrumentation allowed for faster sampling and a greater opportunity to conduct measurements in a region where rough weather often limits ship operations.

Aranda

23 XCPs dropped from the *Aranda* in September 1997 gave an initial overview of the speed, structure and variability of the overflow plume [Gir-

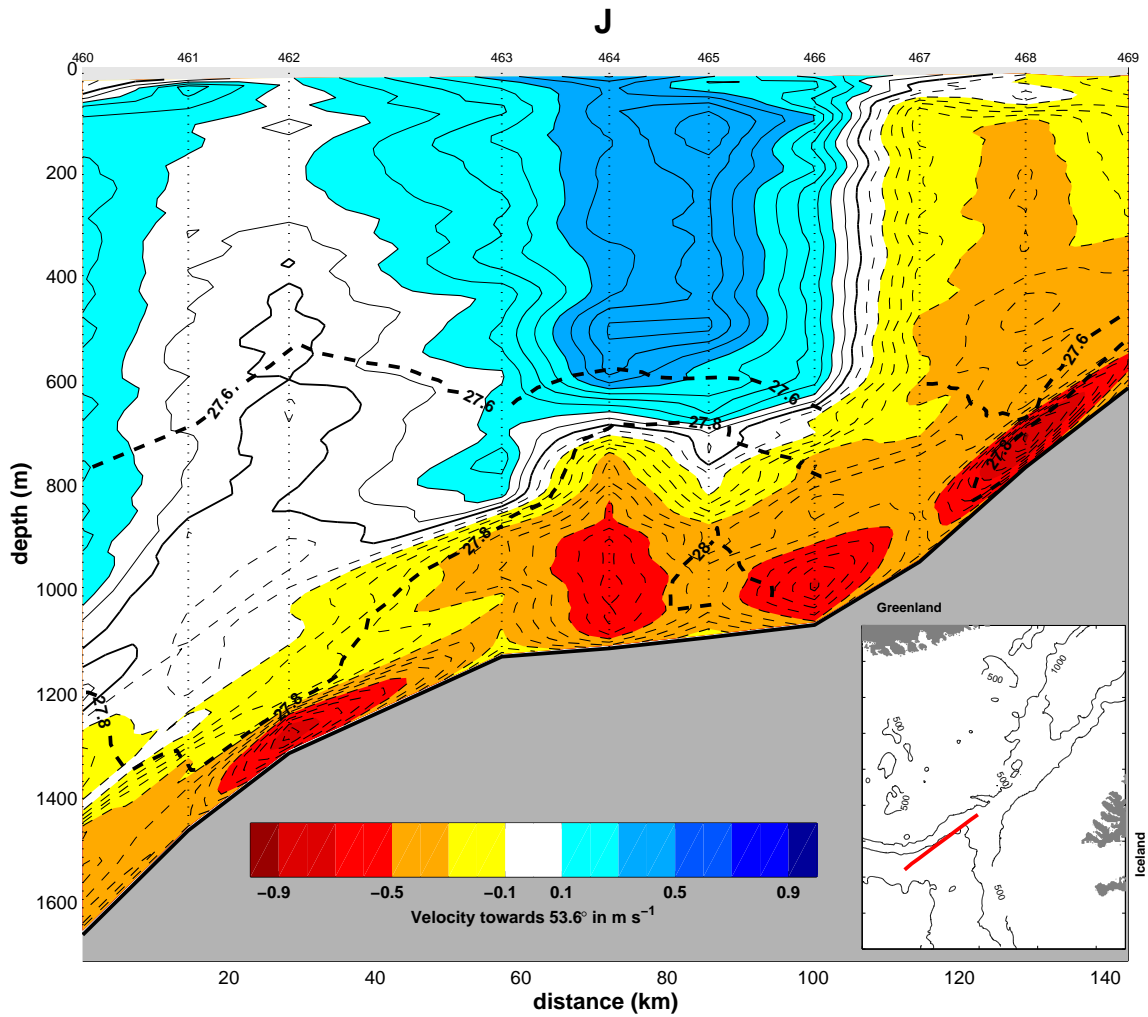


Figure 1. Overflow velocity and density structure from a section along the approximate path of the plume. Profile locations are shown by vertical dotted lines, labeled at the top by station number. Velocity parallel to the section is shaded in color. Density (σ_θ) contours for 27.6, 27.8 and 28.0 kg m⁻³ are shown as dashed lines.

ton and Sanford, 1999]. Bottom-layer velocities as high as 1.4 m s^{-1} and as low as 0.2 m s^{-1} were observed, with thicknesses ranging from 40 to 400 m. A single section along the overflow’s path (Figure 1) showed a sequence of thick domes of dense water with regions of thin overflow layer in-between. The two accompanying cross-stream sections revealed substantial overflow layers, too wide to allow for the interpretation of Figure 1 as a meandering flow. Instead, the domes appear to represent temporal variability in the form of propagating pulses of overflow water.

Poseidon

A more thorough picture of the structure of the overflow was obtained from a 2-week survey on the German research vessel *Poseidon* in 1998 (Figure 2). The survey consisted primarily on a set of full-water-column sections across the overflow path, and, as such, is well-suited to examine the evolution of the plume with distance [Girton, 2001]. Three complete passes were made through the survey region, with the third containing ten cross-plume sections occupied sequentially in the downstream direction. The pattern and magnitude of variability was similar to that seen in the *Aranda* survey and, in fact, the near-sill transport and variability were almost identical to that observed 25 years earlier by a current meter array deployed as part of the OVERFLOW ’73 project [Girton et al., 2001].

Methods

Absolute Velocity

Absolute ADCP velocities were obtained using differential GPS navigation and used to reference the XCP profiles of relative velocity where they overlap. Figure 3a shows a typical example of the very good match between ADCP and XCP-derived velocity profiles. Combined ADCP, GPS and XCP random errors yield a standard error in the estimated water velocity that varies with GPS quality and ship motion but is about 0.02 m s^{-1} for most of the sections discussed here.

Estimating Bottom Stress

Bottom stress is an important parameter affecting the path and speed of a bottom-intensified flow. In the DSO, where instantaneous near-bottom velocities often reach over 1 m s^{-1} , bottom drag may be substantial.

In the turbulent constant-stress layer (or “log layer”) near the bottom, the velocity profile assumes the form

$$u(z) = \frac{u_*}{\kappa} \ln \left(\frac{z}{z_0} \right). \quad (1)$$

Here, u_* is the friction velocity, $\kappa = 0.4$ the von Kármán constant and z_0 the roughness length. A linear fit to a plot of observed u vs. $\ln z$, then, allows a determination of u_* and, hence, shear stress ($\tau = \rho u_*^2$), as shown in Figure 3. The direction of the stress is determined by rotating the velocity components until all of the stress is in one component. Due to the velocity rotation in the planetary boundary layer, this direction is normally to the left of the maximum overlying velocity.

While theoretical and laboratory studies have derived the logarithmic velocity shape for time-averaged velocity profiles, rather than instantaneous ones, the technique has been successfully applied to XCP data a number of times, including in the Mediterranean Outflow [Johnson et al., 1994] and the Faroe Bank Channel [Johnson and Sanford, 1992]. The reason for this success is attributed to the fact that, in general, deviations from the logarithmic shape should only be on the order of the magnitude of u_* , which is usually substantially smaller than the velocity range over the boundary layer. Figure 3 does appear to verify this.

The correct boundary layer height over which to fit remains the subject of some debate. For example, Sanford and Lien [1999] have found systematic differences between stresses estimated from logarithmic fits over the 0–3 m layer vs. the 5–12 m layer, and suggest that the former is the “true” layer of boundary (or wall) turbulence while the latter is dominated by form drag and represents the actual force exerted by the bottom on the flow.

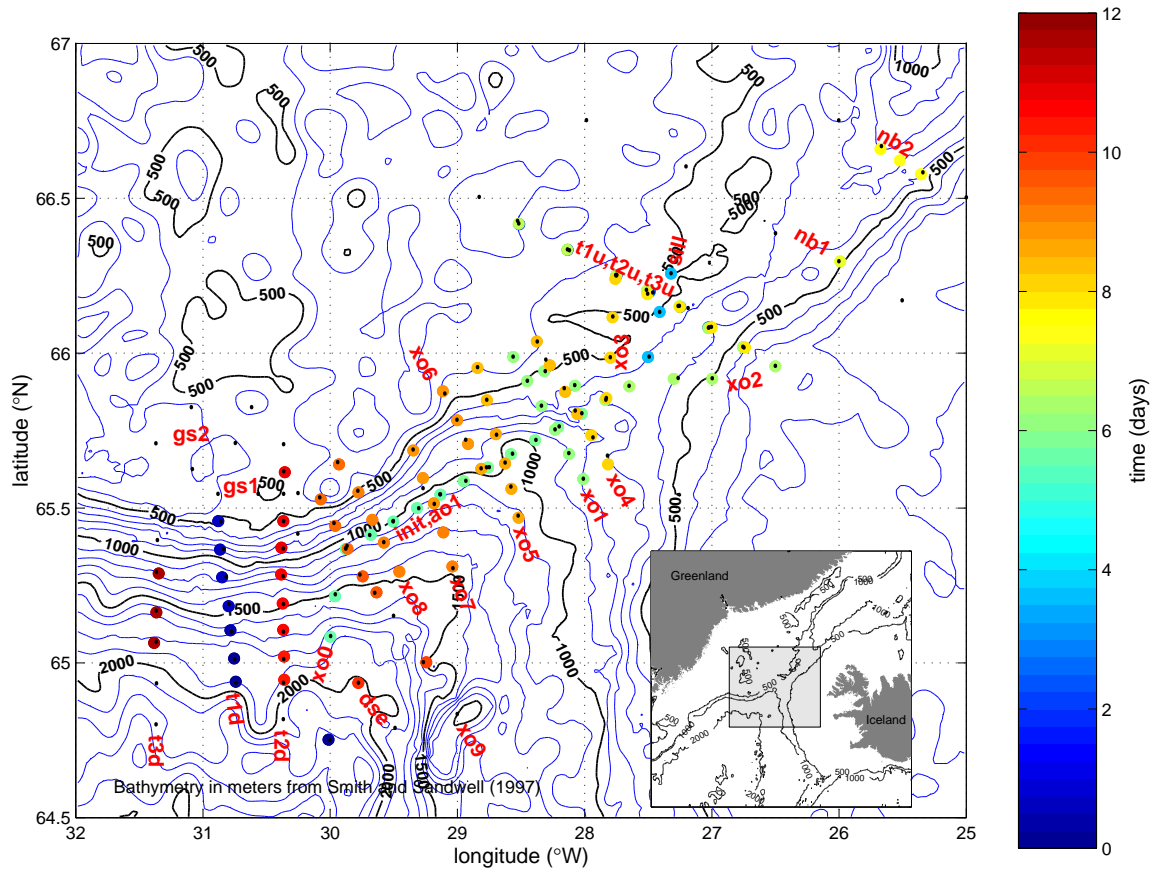


Figure 2. Locations of eXpendable Current Profiler (XCP) drops during *Poseidon* 244 color-coded by time elapsed after the first drop at 0558 UT on September 15, 1998. Note that the sill section and a few other stations contain overlapping symbols, which may be difficult to identify. Stations without XCPs are also shown as small dots. The inset shows the location of the survey in the Denmark Strait, between Greenland and Iceland.

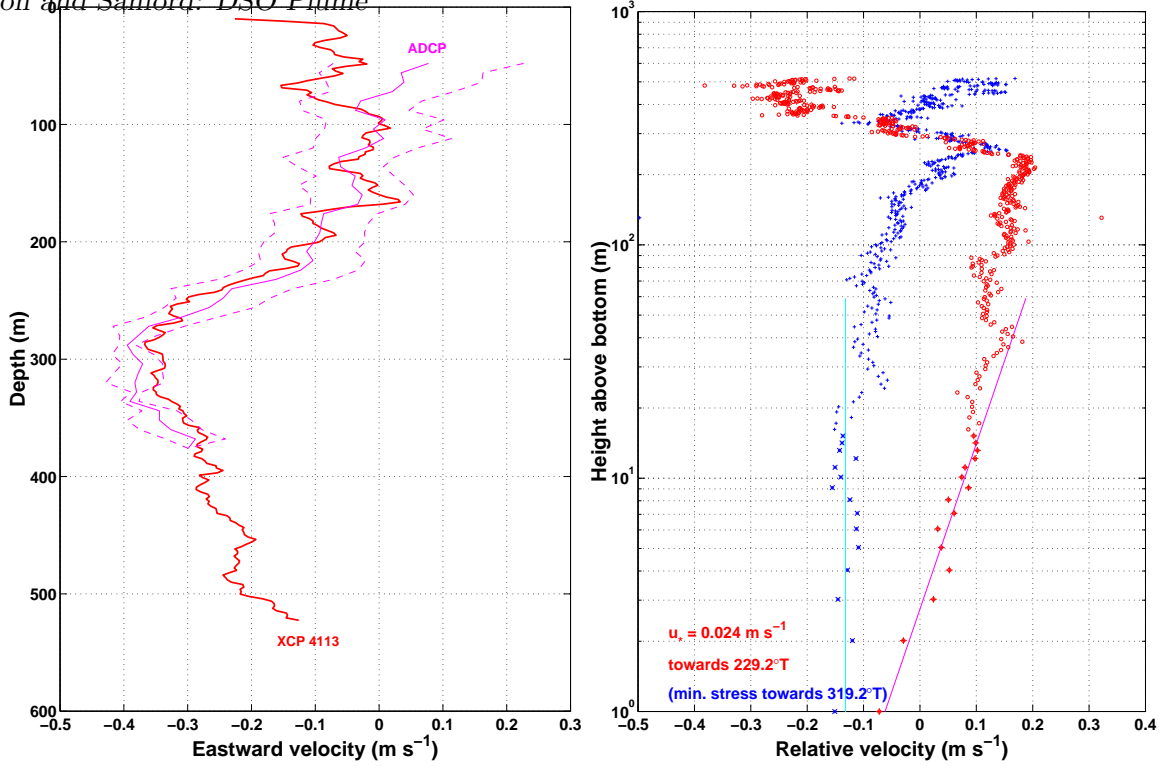


Figure 3. A sample profile showing the good match of XCP and ADCP velocities (left panel) and the logarithmic velocity fit to the bottom 15 m of the XCP (right panel). Both panels are from the same XCP drop (4113), but the left shows the (geographic) eastward component only while the right shows the components in the directions of maximum and minimum log-layer stress.

If this is correct, 0–15 m should give an adequate value for estimating the energy balance of the overflow, and is thick enough so that the XCP yields a suitable number of points to fit.

Streamtube Framework

In its most basic description, the DSO can be thought of simply as a slab of dense water sliding down the continental slope through a stratified background (Figure 4). The flow trades the potential energy it possesses through its density anomaly and height on the slope for downstream kinetic energy, which is in turn a) used to accelerate ambient fluid entrained into the flow and b) extracted by turbulent stresses in the bottom boundary layer.

This one-dimensional approach has been taken by *Smith [1975]*, who described many of the plume-averaged features of the overflow using a simple reduced-gravity, streamtube model. *Price and Baringer [1994]* extended the streamtube description through improved friction and a Richardson

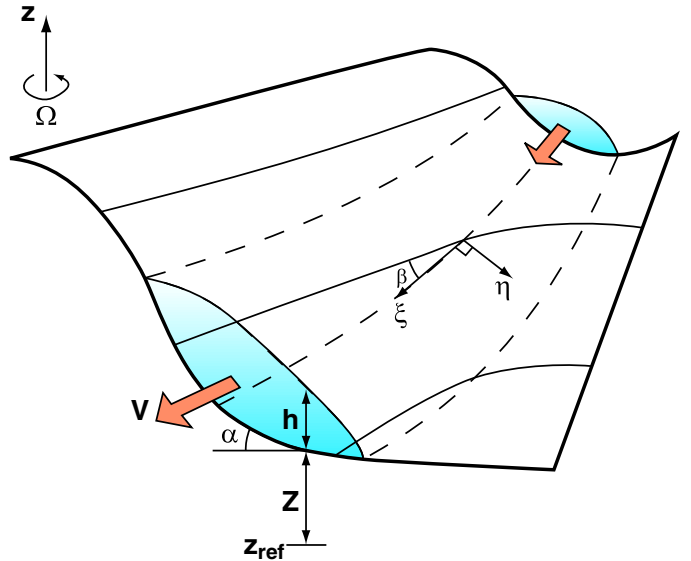


Figure 4. Schematic illustration of the streamtube concept, intended to capture the dominant physics of bottom density currents and overflows.

number-dependent entrainment scheme and applied it to a number of both high- and low-latitude outflows. Of all of these, the DSO is possibly the most problematic because of its highly-variable nature and full-water-column flow.

In the streamtube framework, cross-isobath transport and release of available potential energy (APE) are firmly linked to the overflow's ability to overcome the constraints of geostrophic balance, which tends to prevent APE release. One way for geophysical fluids to release APE is through friction, which reduces velocities and resulting Coriolis accelerations. Figure 5 illustrates how the resulting balance between downslope gravitational force, Coriolis force and retarding friction produces an angled path, with the flow's downward angle decreasing as slope and density anomaly decrease through entrainment or flow into denser background water or less-steep topography. This simple force balance allows the calculation of the rate of plume descent as simply

$$\frac{dZ}{d\xi} = -\sin\alpha \sin\beta = \frac{\tau \cos\gamma}{\rho'gh}, \quad (2)$$

where τ is the magnitude of the combined bottom and interfacial stresses and γ is the angle between the stress and velocity vectors. This is the idealized situation studied with simplified analytical and numerical “streamtube” models [Smith, 1975; Killworth, 1977; Price and Baringer, 1994] and, to a large extent, it is a valid description of the DSO. Applications to date for the DSO have not looked in any detail at the entrainment region that is the focus of this study, but have focused on the steadier regions further downstream, where the streamtube assumptions are arguably more valid.

Deduction of streamtube properties from observed sections

In order to investigate a streamtube description of overflow dynamics from real observations and sampling patterns, it is necessary to make some compromises. The true structure of flow and hydrography involves far more complex patterns than the simple one-dimensional properties

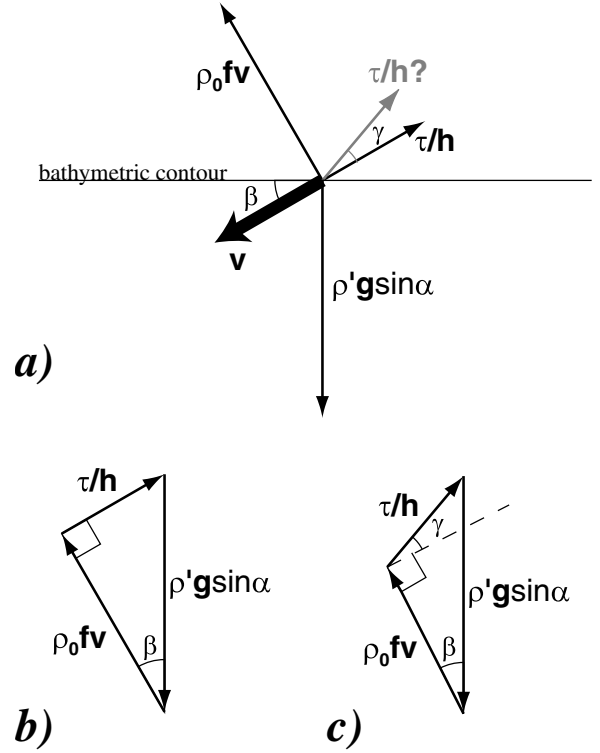


Figure 5. Dominant balance of forces on a 1-D slab-like overflow, illustrating how friction allows descent across bathymetric contours. Panel *c* shows how if the stress (τ) is applied not in the reverse direction to the velocity but at some angle (γ), the downslope angle (β) can be diminished (see Eq. 2).

of the streamtube, so choices in how to average or transform the observations into the desired integral quantities for comparison may have an impact on the credibility of the model. Figure 6 illustrates some of the choices and defines the variables used in the following descriptions.

First of all, I have chosen to define the overflow in terms of density, including all water with $\sigma_\theta > 27.8 \text{ kg m}^{-3}$, following Dickson and Brown [1994].¹ The two most likely problems with a fixed-density definition of the overflow are: 1) a background den-

¹In the discussions which follow, density (ρ) will always refer to potential density referenced to the surface, and $\sigma_\theta = \rho - 1000$. At times it will be convenient to decompose density into a constant mean (ρ_0), stratified background ($\bar{\rho}$) and anomaly (ρ'), as shown in Figure 7.

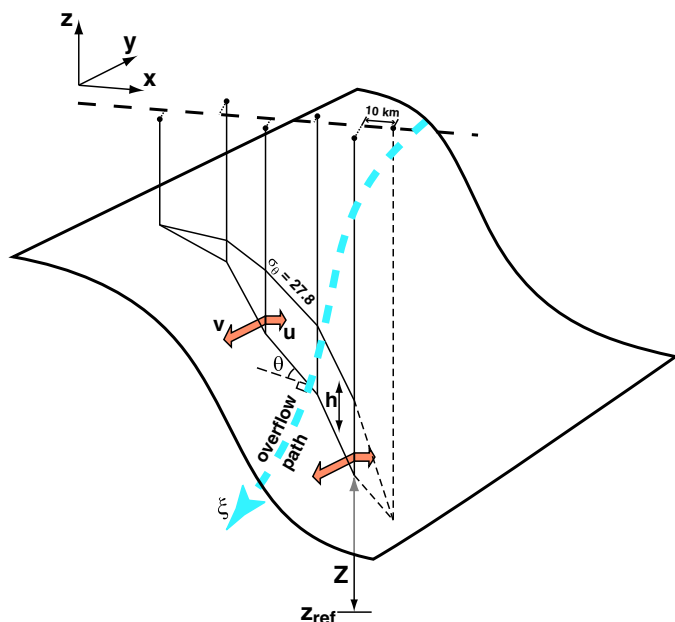


Figure 6. Use of a velocity and water properties section to determine streamtube quantities.

sity approaching the defining isopycnal, leading to an overestimate of transport; or 2) the mixing of overflow water with background water to produce anomalous fluid falling outside of the overflow definition, leading to an underestimate of transport. Fortunately, the $\tilde{\rho}$ profile constructed from stations in the interior of the Irminger Basin does not reach 27.8 kg m^{-3} until 2000 m depth (essentially the maximum depth reached by the overflow in the survey area). As evident from Figure 7, the amount of water between the background density and 27.8 kg m^{-3} is fairly small as long as the bulk of the overflow is sufficiently denser than 27.8 kg m^{-3} . As more mixing occurs, the underestimate of transport due to this intermediate layer could become important. Although both of these effects have the potential to lead to transport errors further downstream where the overflow is less well-defined, in the region described here neither appears to contribute significant errors.

The sections making up our survey were not always perfectly straight lines and were not always perpendicular to the overflow’s path. In order to

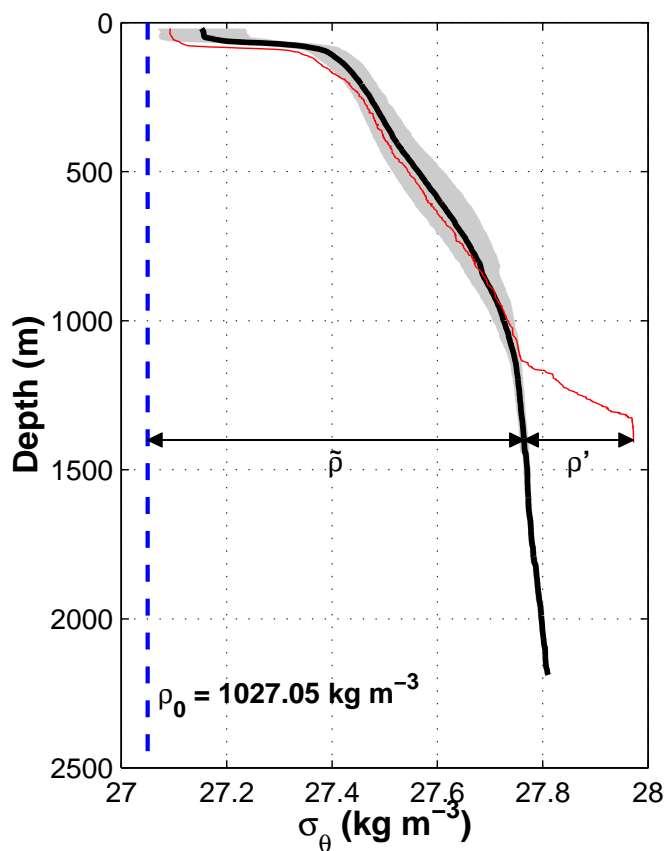


Figure 7. Decomposition of density into mean, background and anomaly contributions. The thin line is a typical overflow density profile. The thick line is the mean background ($\tilde{\rho}$) density profile from several profiles in deep water either above or beyond the boundaries of the overflow water. Gray shading covers the region within 1 standard deviation of the mean.

estimate along-section distance, then, the station positions have all been projected onto a best-fit line for the section. When cross-sectional area is important, the approximate angle, θ , of this line to the flow path normal has been estimated and used as a scaling factor for integrated values. For example, the cross-sectional area of the overflow is

$$A = \cos \theta \iint_A dzdx = \cos \theta \int_W hdx \quad (3)$$

where h is then the thickness of the overflow layer, \int_W denotes integration across the width of the overflow water and \iint_A specifies an integration over the cross-sectional area of the overflow water. In general, most such areal integrations are constructed by deriving averages for the overflow water in each profile, along with thickness h , and then integrating along the section ($\int_W dx$) using the trapezoidal method.

The scaling factor θ is not used when through-section property fluxes are calculated, since the integrated velocity perpendicular to the section is independent of angle. For example, the volume transport of overflow water is

$$Q = \iint_A vdzdx = \int_W \bar{v}hdx, \quad (4)$$

where v is the component of velocity perpendicular to the best-fit section line and \bar{v} is the layer mean for a single profile.

Certain mean quantities for streamtube comparison can be equivalently derived from others, such as an overall velocity

$$V = \frac{\iint_A vdzdx}{A} = \frac{Q}{A}. \quad (5)$$

Many of the results presented in this chapter deal with density-anomaly-weighted averages of various properties, which are compared to the constant properties assumed by the streamtube concept. This approach has been employed using data from a survey of the Mediterranean outflow [Baringer and Price, 1997] with considerable success. Two of the simplest such quantities to define are the position of the center of mass anomaly,

$$X = \frac{\iint \rho'xdzdx}{\iint \rho'dzdx}, \quad (6)$$

and the anomaly-weighted bottom-depth,

$$\bar{Z} = \frac{\iint \rho'Zdzdx}{\iint \rho'dzdx}. \quad (7)$$

Some uncertainty arises when the stations did not span both edges of the overflow water. In these cases, I have chosen to extrapolate the overflow water to zero thickness at a distance 10 km beyond the end of each section but have also generated “error bars” whose lower limit derives from a lack of extrapolation beyond the section and whose upper limit would result from a constant-value extrapolation to 10 km. Large error bars, then, are an attempt to convey the lack of certain knowledge of overflow extent, although in most cases the 10 km extrapolation to zero does appear to be a reasonable guess, with the error bars generally producing (in my opinion) over-estimates of the probable error.

The calculation of mean quantities presents special problems for those values which could tend to disproportionately weight the overflow edges, such as a mean thickness. Even more difficult is an estimate of overflow width, since many sections did not reach the limit of the overflow water at both ends, while most sections did cover the vast majority of overflow volume. One way around this is through the use of a plume “half-width,” $W_{0.5}$, defined such that

$$\int_{X-W_{0.5}}^{X+W_{0.5}} \int \rho'dzdx = \frac{1}{2} \iint_A \rho'dzdx \quad (8)$$

(i. e., the middle 50% of the mass anomaly is contained within a width $W_{0.5}$). A reasonable estimate of the mean thickness is then given by

$$H = \frac{A}{2 \times W_{0.5}}. \quad (9)$$

Results

Pathway and Descent

The geographical distribution of X from all 18 sections is shown in Figure 9 (asterisks), along with

estimates of $W_{0.5}$. Despite the great deal of temporal variability in overflow transport, thickness and velocity, the mean path appears quite stable. Cross-stream variability in X decreases from only 15 km or so within the first 50 km of the sill (the region primarily discussed on Ch. 5) to less than 5 km at the western edge of the domain, just over 220 km from the sill.

As shown in Figure 8, the plume descends relatively slowly at first (during the first 50 km from the sill) and then at a more-or-less constant rate of 6 m km^{-1} .

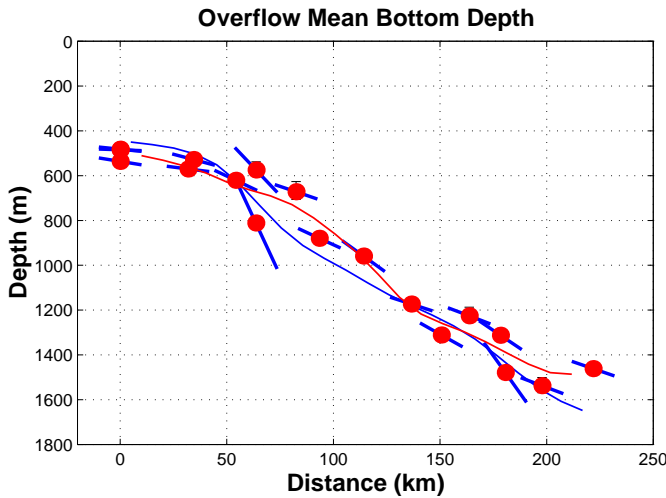


Figure 8. The descent of the overflow with distance from the sill (including sections E and D from the *Aranda* cruise). The red dots show Z , the mass-anomaly-weighted bottom depth of the plume (Eq. 7) for each section. The thick blue angled lines indicate the rate of descent, $\frac{dZ}{d\xi}$, expected from a simple balance between buoyancy, Coriolis force and bottom stress (Eq. 2). The continuous red and blue lines compare the smoothed Z values and a smoothed integration of $\frac{dZ}{d\xi}$, respectively.

The angled bars in Figure 8 show the slope in plume depth *vs.* distance expected from Equation 2, using mean quantities determined at each section (assuming bottom stress to be the primary contributor to τ and applying the measured magnitude of τ_b in the direction exactly opposite to \mathbf{v} —*i. e.*, $\gamma = 0$). If τ_b is permitted to act at an

angle to \mathbf{v} , the resulting rate of descent will be diminished somewhat due to the Ekman veering near the bottom of the velocity profile (Figure 5).

While the bottom stresses, and, hence, the expected rates of descent, do vary considerably from section to section, the plume depth shown in Figure 8 is the result of the integrated history of descent that the flow has undergone since the sill, and so is expected to be substantially smoother than other in-situ properties. This might not be the case, however, if the inhomogeneities in τ were linked to individual water parcels (say, propagating boluses or pulses which carry anomalous water and isolate it from its surroundings). The relative variance in τ and depth, then, holds important implications for the phenomenology of the overflow pulses and sets a limit on the internal isolation of features.

Drag Coefficient The log-fit determined values of bottom stress can be compared to the absolute speed of the water (at 50 m or some other height above the bottom) to estimate a drag coefficient. In aggregate (Figure 10), bottom stress estimates yield $C_D = 3 \times 10^{-3}$, in good agreement with other studies of oceanographic flows. The chosen height of 50 m was intended to be above the boundary layer but still within the overflow water. In fact, due to the frequently large barotropic component of velocity, the mean value of C_D does not depend strongly on the depth chosen.

Experiments with a numerical model described in *Käse and Oschlies [2000]* (hereafter KO), as well as earlier results from simpler models [*Price and Baringer, 1994*], have shown that the pathway of the overflow plume depends strongly on the amount of bottom friction used. The KO model’s (linear) drag coefficient that appears to give the best agreement with the measured pathway, though, yields a substantially lower bottom stress value than the median obtained from our observations.

Slippery Boundary Layers Bottom shear stress is often a dominant process retarding deep currents, but its importance may be reduced in cases where the near-bottom stratification and to-

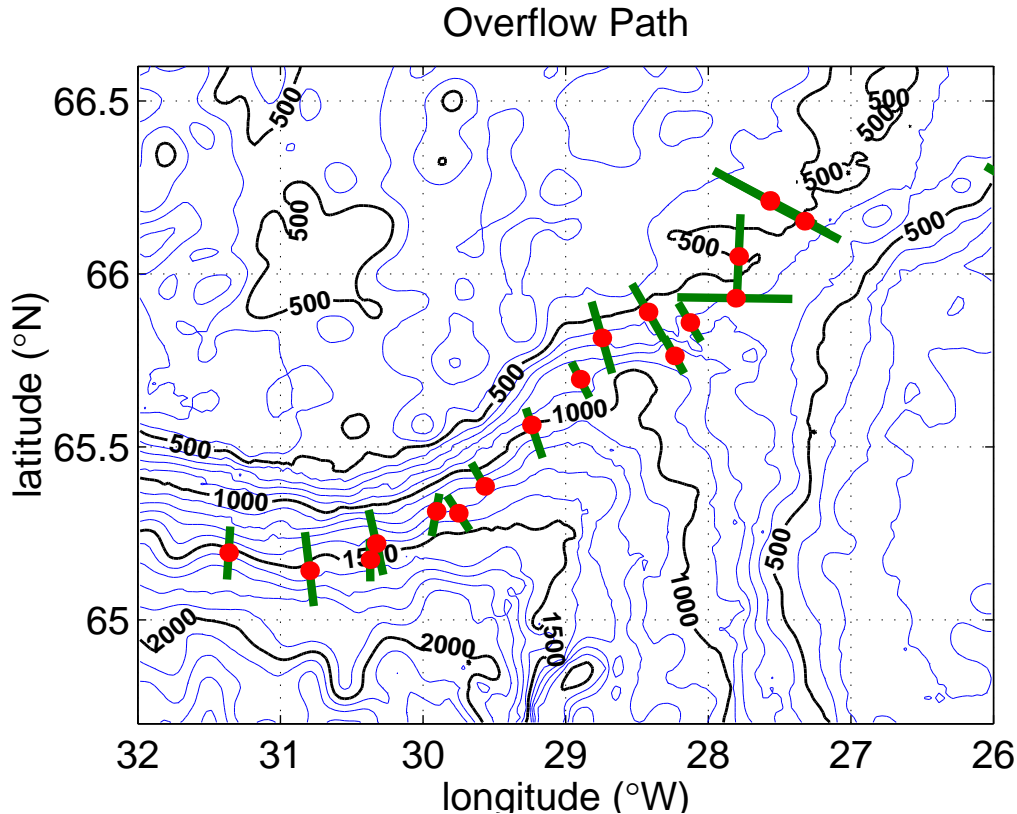


Figure 9. Position of overflow center of mass (X) and half-width ($W_{0.5}$) on each of 18 cross-sections. Apart from some variability at the sill and early in the descent, the flow follows a well-defined path with remarkably little cross-stream scatter.

pographic slope are substantial. As *MacCready and Rhines* [1993] point out, buoyancy transport by the bottom Ekman layer can lead to both a shut-down of the Ekman flow and a reduction in near-bottom velocities through thermal wind shear. This process has the potential to greatly reduce the energy lost to turbulent stresses but may be difficult to detect in the DSO.

For one thing, the interior of the overflow does not appear to be noticeably stratified in the cross-stream direction, making any interior Ekman flow ineffective in producing buoyancy forces. This same difficulty was noted in a survey of the Deep Western Boundary Current at the Blake Outer Ridge (some 6000 km downstream of the Denmark Strait) [*Stahr and Sanford*, 1999]. This appears to point toward a substantial difference between

the type of boundary layer beneath a plume of anomalous fluid entering (under its own power) a stratified ocean and the general case of a boundary layer beneath a stratified current (driven by external forces).

It may still be possible, however, for the stratification at the upslope edge of the plume to contribute to thermal wind shear, reducing stress and further downslope flow at that edge but not at the lower edge. This would contribute to the spreading of the plume, and would also tend to reduce the entrainment of ambient fluid from the upslope edge. For a given topographic slope α and buoyancy frequency N , the Ekman transport process can induce a thermal wind shear of, at most [*Mac-*

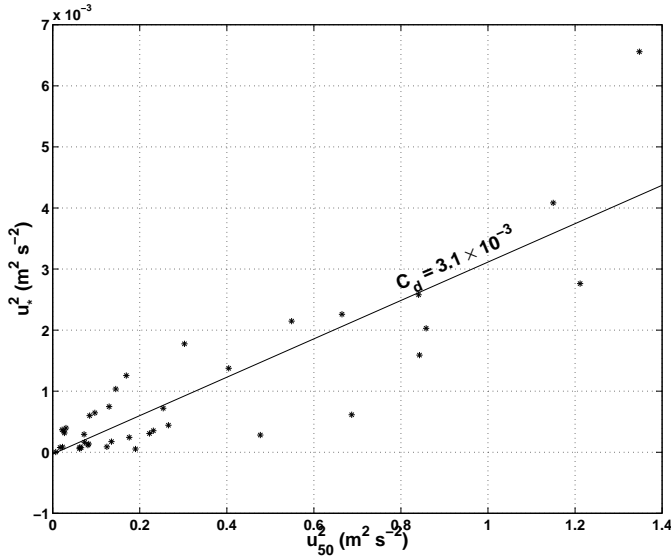


Figure 10. Best guess at C_D from linear fit of u_i^2 vs. u_{50}^2 , where u_{50} is the speed 50 m above the bottom.

Credy and Rhines, 1993],

$$\frac{\partial v}{\partial z_{\max}} = \frac{\alpha N^2}{f} \quad (10)$$

which is set up on a timescale,

$$t = \frac{f}{(N\alpha)^2}. \quad (11)$$

Using values observed near the upper edge of the plume of $N^2 = 2 \times 10^{-5} \text{ s}^{-2}$ and $\alpha = 0.04$ gives a shear of 0.6 m s^{-1} over a 100 m layer and a timescale of just over an hour. In many cases, the observed shears in the near-bottom region are considerably larger than this, particularly in the presence of the strong barotropic currents which tend to dominate the upslope edge of the overflow in the survey region. The short timescale does imply, though, that once the shear reduces to a supportable magnitude, the adjustment could be quite rapid.

Interfacial Stress The stress exerted on the plume at the interface through turbulent momentum transfer (or, equivalently, through the entrainment of slower water) may be an important term

in the momentum balance. Assuming a steady and continuous flow, *Johnson et al. [1994]* used XCP and hydrographic sections across the plume to compute a bulk estimate of the vertical turbulent buoyancy flux, calculated from the residual of mass and volume fluxes, combined with assumptions about the relative magnitudes of buoyancy flux and dissipation. Another attempt to estimate interfacial stress was developed by *Pedersen [1990]* from a compilation of laboratory and field measurements. This method relates stress (τ_i) to an interfacial friction factor (f_i), which can be derived from the Reynolds number (Re_i) through an empirical relation. While Pedersen’s method, designed for steady two-layer flow, may not fully apply in the case of the DSO, it could be compared with bulk estimates.

Other mechanisms for cross-isobath transport Another process which can break the geostrophic constraint and allow APE release and descent across topography is baroclinic instability. However, the potential for linear instability of the DSO in the region of steep plume descent is limited by the magnitude of the slope there [*Swaters, 1991*]. It may be possible that flow instability occurs earlier, over the gradual topography of the sill region. In this case, the inhomogeneities produced near or before the sill could become amplified during the descent of the slope.

Mixing and Momentum

Compounding the loss of potential energy due to its descent, the plume’s density anomaly also undergoes substantial dilution with distance from the sill. This dilution is clearly due to mixing with the surrounding waters, but whether this is through a vertical (diapycnal) process at the interface or more through horizontal (isopycnal) stirring by eddies is not yet entirely certain. In either case, the addition of non-moving ambient fluid acts to reduce the kinetic energy of the flow while conserving momentum. This slowing is termed “entrainment stress.”

If the entrainment process is purely diapycnal, as it must be when the plume boundary intersects

the bottom, it can be parameterized as an entrainment velocity (w_e), representing a net volume influx into the plume through a combination of vertical flow across the boundary (in this case, the $\sigma_\theta = 27.8$ isopycnal) and vertical motion of the boundary itself due to turbulent mixing and redistribution of isopycnals².

Density Changes Both average density,

$$\bar{\sigma}_\theta = \frac{\iint_A (\rho - 1000) dz dx}{\iint_A dz dx}, \quad (12)$$

and density anomaly from the background,

$$\bar{\rho}' = \frac{\iint_A (\rho - \rho_0 - \tilde{\rho}) dz dx}{\iint_A dz dx}, \quad (13)$$

decrease with distance from the sill (Figure 11), with the $\bar{\rho}'$ decrease being, of course, larger due to the increasing background density as the plume descends. The fact that $\bar{\sigma}_\theta$ itself does decrease, however, points to the additional importance of the entrainment of ambient fluid. Although the background stratification ($\frac{\partial \tilde{\rho}}{\partial z}$) decreases from $4 \times 10^{-4} \text{ kg m}^{-4}$ to $6 \times 10^{-5} \text{ kg m}^{-4}$ (N drops from $2 \times 10^{-3} \text{ s}^{-1}$ to $8 \times 10^{-4} \text{ s}^{-1}$) fairly abruptly at around 1000 m, neither the overflow descent nor the rate of ρ' decrease appear to change at this point, while the rate of σ_θ decrease appears to become steeper. A simplistic estimate of average entrainment velocity is:

$$w_e = \frac{VH}{\bar{\rho}'} \frac{d\bar{\sigma}_\theta}{d\xi}, \quad (14)$$

where ξ indicates the downstream coordinate, as shown in Figure 4. Using the slopes shown in Figure 11 to estimate $\frac{d\bar{\sigma}_\theta}{d\xi}$ for the two regions above and below 1000 m (~ 125 km from the sill), combined with mean values of V , H and $\bar{\rho}'$ in each region, indicates more than an order of magnitude increase in w_e from $6 \times 10^{-5} \text{ m s}^{-1}$ before 125 km to

²In fact, due to the isopycnal definition of the boundary, this interpretation could cause problems if there is substantial mixing between the boundary fluid itself and the background, producing anomalous fluid “outside” the plume.

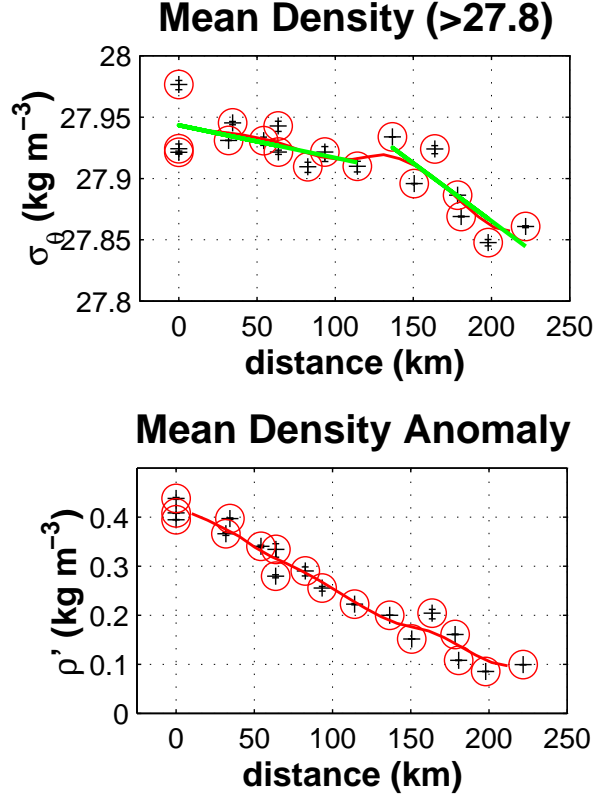


Figure 11. Evolution of plume density ($\bar{\sigma}_\theta$) and density anomaly ($\bar{\rho}'$) with distance from the sill. The solid red line is from a smoothing of the points with a 20 km Gaussian window. The two green lines in the left-hand panel are from linear fits to the regions before and after 125 km, and seem to show a significant change in slope.

$8 \times 10^{-4} \text{ m s}^{-1}$ after 125 km. This increase could be the result of a decrease in bulk Richardson number,

$$\text{Ri}_b = \frac{\bar{\rho}' g H}{\rho_0 V^2}, \quad (15)$$

as the plume anomaly decreases (average $\bar{\rho}'$ goes from 0.34 kg m^{-3} to 0.14 kg m^{-3}) and thickness increases (average H goes from 150 m to 240 m). However, the large variability in thickness and velocity make the significance of this decrease difficult to determine. Estimates from section-averaged quantities do show a larger fraction of $\text{Ri}_b < 1$ values beyond 125 km from the sill and the mean Ri_b over the regions before and after 125 km are 1.8 and 1.2, respectively. Another possibility is that

it is the decrease in background stratification itself which is responsible for this increase in entrainment. While the large stratification at the layer interface has been the focus of most investigations, the weaker stratification above the interface might have an influence on the shape and penetration of the eddies which drive the entrainment.

Even the lower estimates of w_e above are an order of magnitude higher than values estimated from the few existing microstructure measurements in the Denmark Strait [Oakey and Elliott, 1980]. Although these measurements were far from comprehensive in coverage, they did estimate vertical diffusivities (K_z) resulting from temperature microstructure and determine that microscale turbulent processes alone are insufficient to account for the bulk w_e estimates of Smith [1975] (which are on the order of 10^{-4} m s^{-1} —smaller than the downstream region of this study).

In addition to its consequences for overflow mean density, w_e should have a profound effect on transport changes resulting from the inclusion of new water. Figure 12 shows the through-section transport (Q) of $\sigma_\theta > 27.8 \text{ kg m}^{-3}$ water on all sections, demonstrating that the effect of entrainment may be particularly difficult to pick out of the short-term variability present in the measurements. Although the integrating effect mentioned above in Section 3 should apply to total transport as well, the constituent measurements of velocity (V) and cross-sectional area (A) are themselves highly variable (see Figure 13). In fact, a substantial fraction of total transport may be due to the co-variability of these quantities, casting further doubt on the simplified streamtube model.

Immediately, complications come to mind due to the fact that the overflow does not, in fact, have only a single velocity and density, and the overlying water is neither motionless nor uniform in structure from station to station. However, it is important to know how close the reality comes to following these idealized models and whether the dominant force balances are as they describe.

Energy Changes As mentioned previously, the energy source for the overflow is the potential

energy (PE) of the density anomaly due its thickness (internal potential energy—iPE) and height on the slope (external potential energy—ePE). Energy terms are calculated as follows:

$$\text{KE} = \frac{1}{2} \int_W \rho_0 |\mathbf{u}|^2 h dx \quad (16)$$

$$\text{iPE} = \frac{1}{2} g \int_W \rho' h^2 dx \quad (17)$$

$$\text{ePE} = g \int_W \rho' h Z dx \quad (18)$$

Previous studies of oceanic outflows—particularly from the Mediterranean [Johnson *et al.*, 1994; Baringer and Price, 1997]—have suggested that the loss of potential energy is primarily accounted for by frictional stresses at the ocean bottom and plume interface. The expected streamtube momentum balance gives

$$\frac{d}{d\xi} (\text{KE} + \text{iPE} + \text{ePE}) = - \int_W (\tau_b + \tau_i) d\eta. \quad (19)$$

In terms of their contribution to the along-stream momentum budget, frictional forces applied over the surface of the plume should produce changes in total energy with downstream distance. Figure 14a shows the total energy (TE = KE + iPE + ePE) measured at each section as well as the expected slope ($\frac{d}{d\xi}(\text{TE})$) from bottom stress measurements alone. While the section-to-section variability makes a definitive statement difficult, there does appear to be a decrease in TE with distance, primarily due to the descent of the plume and subsequent loss of ePE. The major sink of ePE appears to be frictional losses. The exception to this pattern is clearly the high ePE and iPE of the sill sections (t1u, t2u, t3u) which does not appear to carry over into the downstream sections. In fact, the sill sections do not release all of their APE into the downslope overflow, in part, due to the presence of a cross-strait geostrophic (baroclinic?) flow which holds the dense water back. This same effect has been seen in the KO model, with the cross-strait current contributing to both recirculating flow in the northern basin and to the southwestward-flowing East Greenland Current on

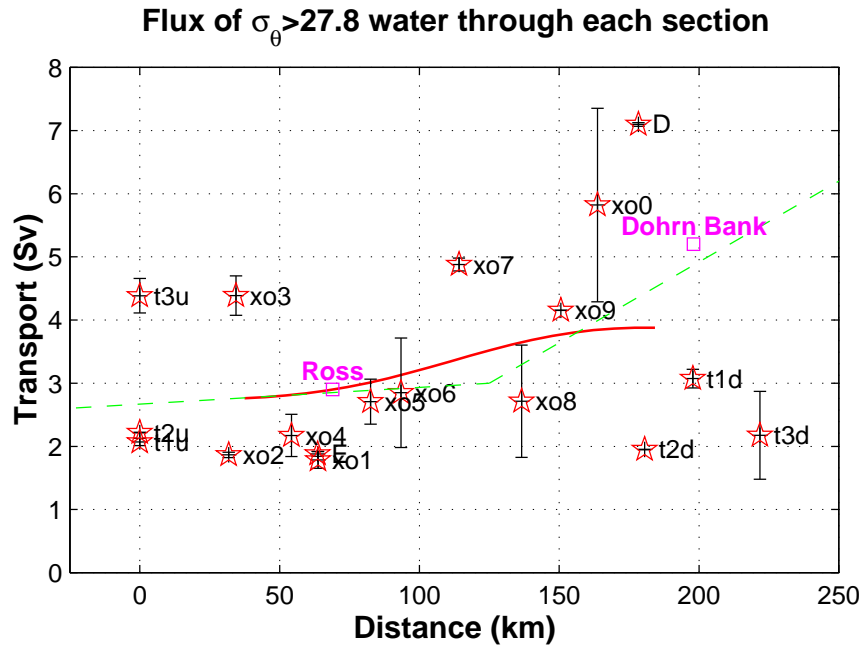


Figure 12. Dense water transport (Q) vs. distance from the sill, as measured by all 18 sections with XCPs (including two from the *Aranda*) as well as two current meter arrays (labeled as “Ross” and “Dohrn Bank”). The dashed lines show rates of transport increase expected from constant w_e values of $6 \times 10^{-5} \text{ m s}^{-1}$ and $8 \times 10^{-4} \text{ m s}^{-1}$ (estimated from Eq. 14 and Fig. 11 lines) over widths of 44 km and 32 km (average values of $2 \times H_{0.5}$ in the regions before and after 125 km, respectively). The solid curve is from a smoothing of the Q values with a 75 km Gaussian filter.

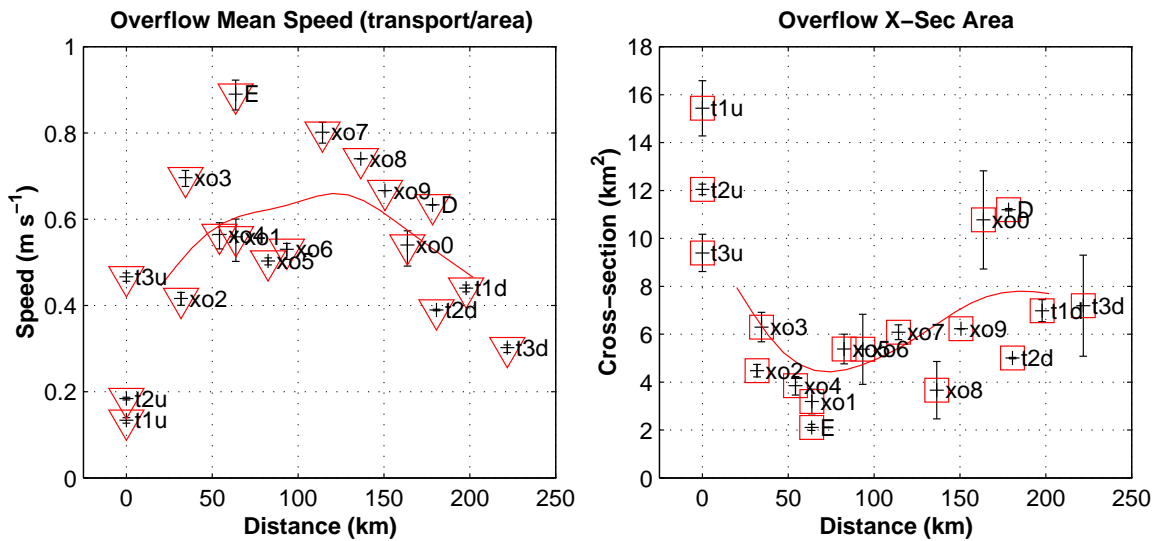


Figure 13. Variability of plume velocity (V) and cross-sectional area (A) over distance from the sill. See Equations 5 and 3 for definitions of these section-averaged quantities. Curves show smoothed versions using a 40 km Gaussian window.

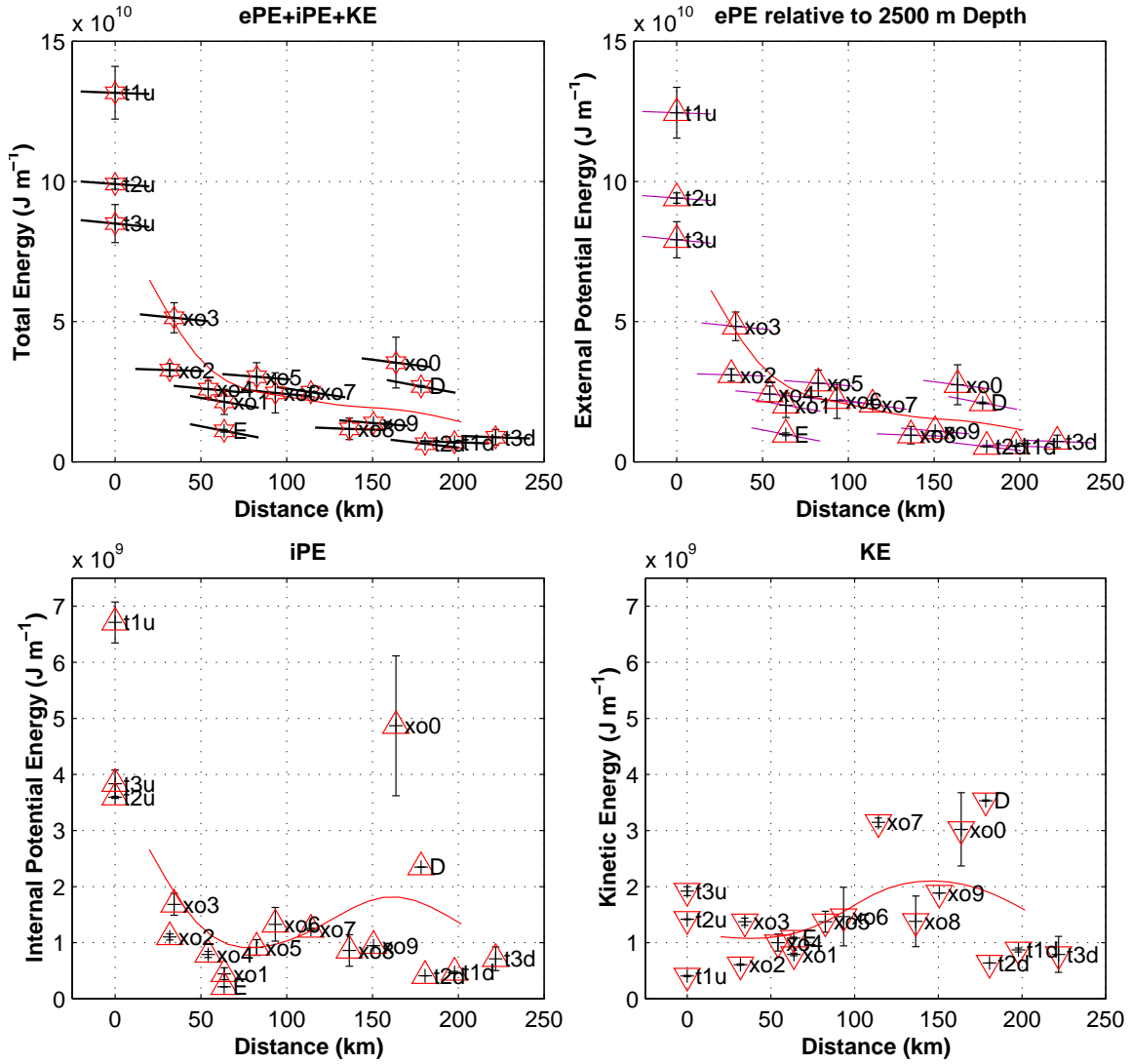


Figure 14. Evolution of energy terms with distance from the sill. Note the exponent in the y -axis, with the energy range of the upper two panels a factor of 20 greater than the lower two. The sloping lines on upper-left panel indicate rate of energy loss expected from bottom friction measurements at each section, as determined from Eq. 19 (and neglecting τ_i). Solid curves are the values smoothed with a 40 km Gaussian window.

the shelf. It appears that the intermittency of this front is responsible for (or a consequence of) the majority of the variability in the downstream flow. It is important to note that the possibility of an along-stream pressure gradient is generally ignored in the 1-D streamtube models of *Smith* [1975] and *Price and Baringer* [1994].

Clearly, the streamtube approach is not an appropriate way to connect observations at the sill with those in the overflow downstream. Instead, the continuity of energy *flux*, which requires fewer assumptions about flow behavior, will be considered in Section .

Entrainment Stress Using the rough estimates of w_e from Section it is possible to estimate the effective mean entrainment stress as $\tau_i = \rho_0 V w_e$, where V is the streamtube velocity [*Price and Baringer*, 1994]. Taking 0.6 m s^{-1} as a reasonable mean velocity over the entire region (from Figure 13), the τ_i values estimated in the low-entrainment and high-entrainment regions are 0.04 Pa and 0.8 Pa, respectively. These can be compared to the overall mean section-averaged bottom stress (τ_b) of 1.7 Pa (where section-averages range from 0.5 Pa to 4 Pa on individual sections). If the high-entrainment region diagnosed from σ_θ changes is, in fact, a real feature of the DSO, then it is clear that entrainment stress could play a significant role in the momentum balance of this region.

Energy Flux

In order to examine the effects of bottom friction and entrainment stress on the overflow without having to resort completely to the assumptions of a streamtube model, it may be helpful to examine the energy flux carried by the flow. I will still proceed by assuming that there is a more-or-less continuous flow from the sill along the Greenland slope. I will then attempt to relate along-stream changes in total flux to processes occurring within and at the boundaries of the overflow. Energy partition changes will also be examined. The nature of residuals will not be known exactly, but can be related to bottom friction and entrainment stress as estimated by previously-mentioned means.

The advantages of a flux-based approach are that the flux through a section is made up of the areal integral of the perpendicular component of the flux vector and so should not depend very strongly on the angle of the section to the flow. In addition, cross-sectional variations in thickness, density and velocity can be included in the total flux to give a more accurate representation. A major disadvantage to interpreting energy flux is the additional variability produced by an extra factor of velocity included in most of the terms.

Following Gill, the kinetic energy equation is derived from the dot-product of \mathbf{u} with the momentum equation, giving:

$$\frac{\partial}{\partial t} \left(\frac{1}{2} \rho |\mathbf{u}|^2 \right) + \nabla \cdot \mathbf{F} = -wg\rho - \rho\epsilon, \quad (20)$$

where $\mathbf{F} = (p + \frac{1}{2}\rho|\mathbf{u}|^2)\mathbf{u} - \mu\nabla(\frac{1}{2}|\mathbf{u}|^2)$ is the mechanical energy flux density. Note that the KE flux includes not only the advective flux of KE but also a viscous flux and a pressure flux. While molecular viscosity can probably be neglected, the effects of bottom and interfacial stresses can be included by substituting an eddy viscosity for μ (rather than trying to include turbulent fluctuations in u and p). Adding in the potential energy equation,

$$\frac{\partial}{\partial t}(\rho\Phi) + \nabla \cdot (\rho\Phi\mathbf{u}) = wg\rho \quad (21)$$

(where Φ , the geopotential, is defined by $\nabla\Phi = g\hat{\mathbf{k}}$ and so contains an arbitrary reference height), removes the vertical velocity term, giving the total energy equation:

$$\frac{\partial}{\partial t} \left(\rho \left(\Phi + \frac{1}{2} |\mathbf{u}|^2 \right) \right) + \nabla \cdot \mathbf{F}^{\text{tot}} = -\rho\epsilon, \quad (22)$$

where $\mathbf{F}^{\text{tot}} = \rho\mathbf{u} \left(\Phi + \frac{1}{2} |\mathbf{u}|^2 + \frac{p}{\rho} \right) - \mu\nabla \left(\frac{1}{2} |\mathbf{u}|^2 \right)$ is the total energy flux density.

The conservation of total energy within a volume then comes from the volume integral of 22, giving:

$$\frac{\partial}{\partial t} (K + P) + \iint_S \mathbf{F}^{\text{tot}} \cdot \hat{\mathbf{n}} dS = \iiint_V (-\rho\epsilon) dV, \quad (23)$$

where $K = \iiint_V \frac{1}{2} \rho |\mathbf{u}|^2 dV$, $P = \iint_S \rho \Phi dS$, and $\iint_S()dS$ and $\iiint_V()dV$ indicate surface and volume integrals, respectively.

The volume in question is bounded by the $\sigma_\theta=27.8$ isopycnal surface and the ocean floor, and we expect that $\frac{\partial}{\partial t}(K + P) = 0$ over an interval of a few days or longer (as supported by the stable means of long-term current meter records *Dickson and Brown* [1994]; *Ross* [1984]). If we assume that the dissipation rate (ϵ) is much smaller than the throughput of energy flux, we are left with a balance between downstream changes in flux through vertical cross-sections and fluxes through the top and bottom of the volume. As pictured in Figures 4 and 6, the coordinates parallel to and perpendicular to each section are x and y (unit vectors \hat{i} and \hat{j}), while the idealized along-stream coordinate (often plotted as “distance from the sill”) is ξ .

Since a steady state is only expected to hold in the mean, it is likely that fluctuating components do contribute to the time-mean flux. Any such fluctuating flux in the cross-stream direction (due, for example, to the radiation of internal waves) will only appear as part of the residual of along-stream flux changes.

The energy lost to bottom friction can be evaluated from the integral over the bottom surface of the overflow of the turbulent form of the $-\mu \nabla \cdot (\frac{1}{2} |\mathbf{u}|^2)$ term in \mathbf{F}^{tot} . Noting that the turbulent stress $|\tau_{\mathbf{b}}|$ takes the place of the viscous stress $\mu \frac{\partial |\mathbf{u}|}{\partial z}$ and neglecting horizontal derivatives and vertical velocities gives:

$$-\mu \nabla \cdot (\frac{1}{2} |\mathbf{u}|^2) \approx -\mu \frac{\partial}{\partial z} (\frac{1}{2} |\mathbf{u}|^2) \quad (24)$$

$$\approx -\mu |\mathbf{u}| \frac{\partial |\mathbf{u}|}{\partial z} \quad (25)$$

$$\approx -|\tau_{\mathbf{b}}| |\mathbf{u}|. \quad (26)$$

Over a distance $\Delta \xi$ along the overflow, bottom friction will contribute an amount $-\Delta \xi \int_W |\tau_{\mathbf{b}}| |\mathbf{u}| dx$ to the surface integral of $\mathbf{F}^{\text{tot}} \cdot \hat{\mathbf{n}}$. Alternatively, loss to bottom friction alone should result in a balance of

$$\frac{d}{d\xi} \iint_A (\mathbf{F}^{\text{tot}} \cdot \hat{\mathbf{j}}) dz dx = \int_W |\tau_{\mathbf{b}}| |\mathbf{u}| dx. \quad (27)$$

This rate of change is shown by the slopes of the lines in Figure 16. A similar term resulting from entrainment stress could also be added.

The total energy flux through an overflow cross-section, $\hat{n} = \hat{j}$, is made up of the sum of 6 terms:

$$\begin{aligned} \iint_A (\mathbf{F}^{\text{tot}} \cdot \hat{\mathbf{j}}) dz dx &= [\#1] \frac{1}{2} \int_W \rho_0 v |\mathbf{u}|^2 h dx \quad (\text{KE}) \\ &+ [\#2] g \int_W \rho' v h^2 dx \quad (\text{iPE} \times 2, \text{includes} \\ &+ [\#3] g \int_W \rho' v h Z dx \quad (\text{ePE}) \\ &+ [\#4] \frac{1}{2} g \int_W \tilde{\rho} v h^2 dx \quad (\text{iPE} - \text{like}) \\ &+ [\#5] g \int_W \tilde{\rho} v h Z dx \quad (\text{ePE} - \text{like}) \\ &+ [\#6] g \int_W [v \int_H (\int_z^0 \tilde{\rho} dz) dz] dx \quad (\tilde{\rho} \mathbf{u} \text{ term}) \end{aligned}$$

where v is the velocity component normal to the section, h is the overflow layer thickness, Z is the bottom height relative to a reference depth of 2500 m, \int_W and \int_H indicate integrals over the width and thickness of the overflow, respectively, and ρ has been decomposed into a constant mean ($\rho_0 = 1027.2 \text{ kg m}^{-3}$), stratified background ($\tilde{\rho}(z)$) and plume anomaly (ρ').

The first three terms are simply the through-section flux of the quantities plotted in Figure 14, with the exception that the iPE term (#2) is doubled due to the addition of an identical pressure term from the KE equation (20). The last three terms are contributions of the stratified background and represent both the downslope flow of background density from one region into another and the increase of internal energy due to the increasing pressure of the stratified background. The six terms are shown separately in Figure 15, and the total through-section flux is shown in Figure 16, along with the downstream decrease rate expected from $\tau_{\mathbf{b}}$ measurements.

Trends are difficult to pick out of the substantial scatter in the energy flux terms. Any change in total energy flux (Figure 16) is, if anything, less significant than the change in overflow volume transport (Figure 12) which is already clearly under-sampled. The dominant energy flux terms include

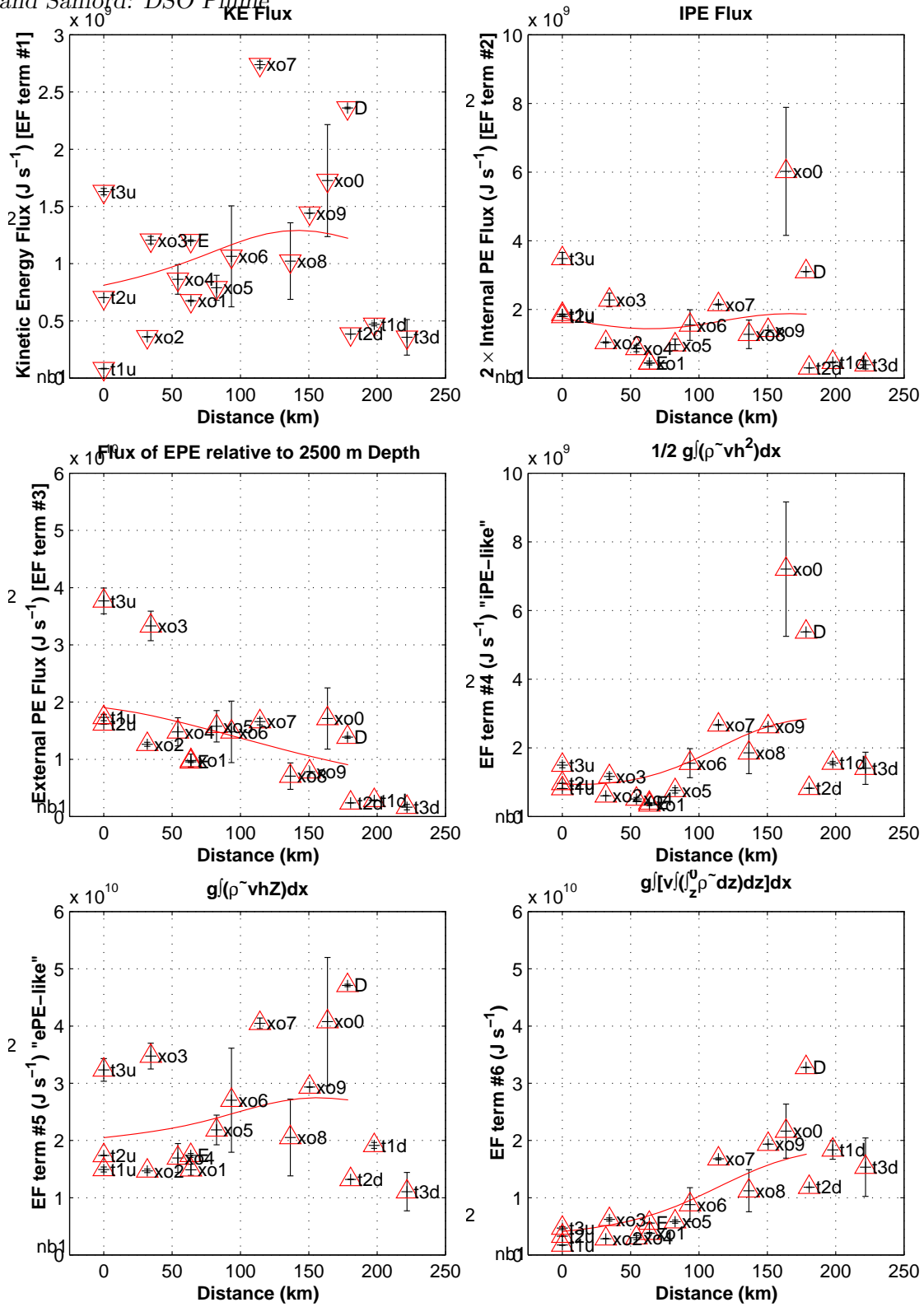


Figure 15. Through-section energy flux vs. downstream distance. Each panel shows one of the six terms in $\iint_A (\mathbf{F}^{\text{tot}} \cdot \hat{\mathbf{j}}) dz dx$. Curves were smoothed with a 75 km Gaussian window.

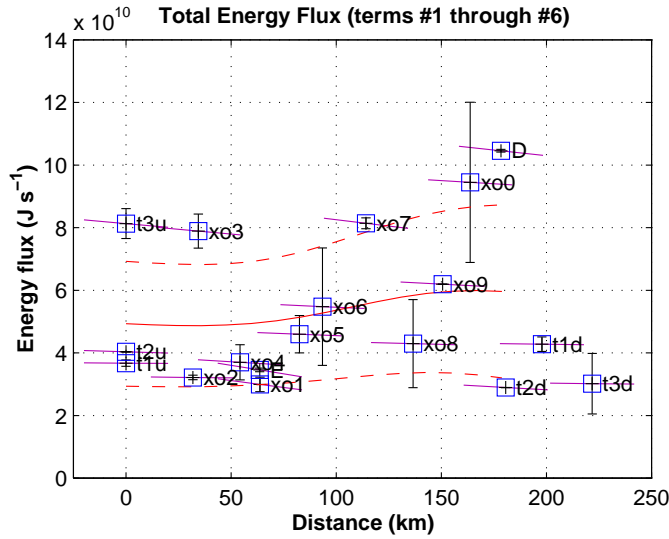


Figure 16. Total energy flux ($\iint_A (\mathbf{F}^{\text{tot}} \cdot \hat{\mathbf{j}}) dz dx$) observed at each of 18 sections across the overflow. Values plotted are the sum of all six panels in Fig. 15. Slanted lines at each section indicate the rate of decrease expected from bottom stress measurements (Eq. 27). The solid curve is a smoothing of the energy flux values using a 75 km Gaussian window, with the dashed curves indicating the envelope of 1σ variance (weighted with the same filter).

ePE (#3) and two of the background terms (#5 and #6), indicating that the bulk of the ePE flux decrease is taken up by the work against the background stratification. Despite flux divergence due to bottom friction (shown in Figure 16) as well as additional loss to entrainment stress and possibly wave radiation, the total energy flux appears to *increase*. This is difficult to say with certainty, but could indicate the influence of an external pressure gradient (either due to surface slope or variations in the water above the overflow) that is tending to accelerate the flow. One clue to the existence of such a gradient is the cross-strait flow at the sill. Although such an external gradient has been explicitly ignored in the streamtube model, it may be a direct consequence of the hydraulic control and barotropic dynamics at the sill, and would provide a source of increasing energy flux.

Another feature of the total energy flux apparent in Figure 16 is a downstream increase in the envelope of variability. This increase may indicate a steepening of the flux-carrying features in the overflow as they propagate downstream. This argues in favor of an instability or nonlinear process affecting the evolution of the flow through internal flux convergences. Some of this increase in variability envelope is also apparent in the smaller individual terms #1 and #2, indicating that at least part of the process includes both a conversion of potential to kinetic energy and a steepening in overflow interface excursions as might be expected from a soliton-type wave.

Inertial Wave Drag In rotating laboratory experiments, much of the energy lost during the descent and geostrophic adjustment of a dense turbulent plume on a slope is through the radiation of inertial waves [Griffiths, 1983]. This effect has not been observed in the field (*e.g.* the Mediterranean outflow) but may still be an important effect controlling the rates of adjustment and decay. Before this can be determined, a survey of inertial wave energy must be included in the overflow energy budget.

Discussion

One of the goals of the intensive study in the entrainment region of the DSO is to elucidate the mechanism behind the dramatic increase of transport noted by *Dickson and Brown* [1994] from 2.9 Sv near the sill to 5.2 Sv at the Dohrn Bank array, 160 km downstream. As shown by Figure 12, our measurements do yield the appropriate amount of entrainment to gain this increase, despite the fact that the transport measurements from the survey are heavily aliased by temporal variability.

The possibility of an alternate pathway for some of the flow which misses the O73 current meters but rejoins before the Dohrn Bank array has been suggested by some hydrographic surveys [*Rudels et al.*, 1999]. However, this option is not necessary unless the overflow entrainment is significantly weaker than suggested by our bulk estimates of w_e based on the dilution of the plume with distance from the sill. In addition, the pathway of the majority of the overflow water, shown in Figure 9, exhibits strikingly little meandering behavior, despite the large variations in transport. This steady pathway does not leave much room for extra branches high on the shelf.

A question that has not been answered by our study is the relative importance of vertical and horizontal processes in the dilution of the plume. A strong candidate for the entrainment mechanism is the more-or-less straightforward process of turbulent overturns driven by shear instability, possibly combined with stationary hydraulic jumps at locations of steep ridges or canyons in the topography. However, it is also quite possible that the flow variability in the form of eddies and downslope subplumes [*Jiang and Garwood*, 1996] contributes substantially to the mixing of the fluid with the surrounding water. Although our definition of the overflow using an isopycnal surface implies that some sort of diapycnal process is required to produce entrainment, stirring by eddies could play a large role in enhancing this process through additional stretching and folding of material surfaces.

Conclusions

Girton et al. [2001] showed that there has been little change in either the magnitude of transport or the pattern of variability of the overflow between surveys in 1973 and 1998. Once this agreement over a 25-year period is established, it becomes more plausible that significant features observed in the recent surveys can be considered universal characteristics of the DSO. In particular, the evolution of streamtube-averaged properties is important for diagnosing the forcing and modification the overflow undergoes in its path to becoming North Atlantic Deep Water.

In aggregate, the set of velocity and hydrography sections collected on the *Poseidon* and *Aranda* cruises considered in the context of a streamtube description do capture a “zeroth-order” picture of certain properties and dominant balances of the overflow. In particular, the pathway and descent of the plume are relatively constant over the first 250 km from the sill, and appear to be dominated by topography and bottom stress. The path of the dense water as it descends the Greenland continental slope has surprisingly little variability, following a path of essentially constant rate of descent over topography consistent with a balance between buoyancy, Coriolis acceleration and stress at the bottom of the dense plume.

The mean plume density steadily decreases throughout the descent, with an apparent break in slope at ~ 125 km. This points to increased entrainment in the latter half of the survey area. The increase could be due to the larger topographic slopes in this region (see Figure 17), in combination with the loss of density anomaly as the plume enters deeper water. Average Richardson numbers in these two regions do indicate less stability (and, hence, the likelihood of greater entrainment) in the latter region, but the difference is small. Also, at 125 km from the sill: the plume-averaged mean velocity reaches a maximum; the plume encounters an abrupt reduction in background stratification at approximately 1000 m depth; and the rate of density change with distance in the plume increases,

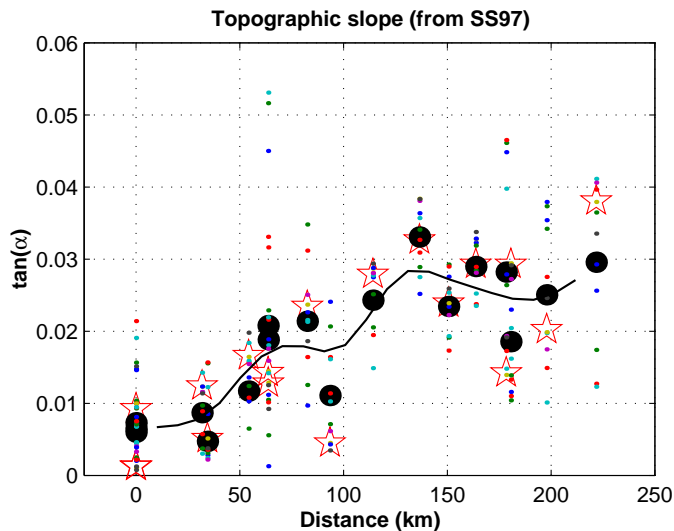


Figure 17. Topographic slopes at each section computed from SS97 bathymetry. Large dots show the average slope across the width of each section. Stars indicate the slope under the center of overflow mass anomaly. Small dots are the slope at each station, indicating the range of slopes over each section. The solid curve is a smoothing of the average slopes using a 20 km Gaussian window.

suggesting an increase in entrainment velocity (w_e) from $6 \times 10^{-5} \text{ m s}^{-1}$ to $8 \times 10^{-4} \text{ m s}^{-1}$.

Other properties, such as V , A and Q have much higher levels of variability, and are not quite so readily interpreted. The eddies responsible for this variability will be discussed in a later publication.

The energy partitioning of the plume is dominated by “external potential energy” (ePE) due to the position of the density anomaly on the slope, which decreases in the downstream direction due to friction. However, the sections at the sill have a much higher ePE than those on the slope, implying that not all PE at the sill is released into the overflow.

Energy *flux* through the sill sections is consistent with the flux downstream, demonstrating the continuity of the overflow, even if not all potential energy present at the sill is released into the plume.

The energy flux is also dominated by ePE as well as by the pressure resulting from the descent

into a stratified background.

Although there is substantial variability, the total energy flux appears to increase or at least steepen with distance from the sill (as shown by the increasing envelope of Figure 16). An increase in the mean flux could imply additional forcing by, for example, a surface pressure gradient. The increasing envelope is likely related to the evolution of the eddies in their transit through the survey region.

References

- Aagaard, K., and S.-A. Malmberg, Low-frequency characteristics of the Denmark Strait Overflow, in *ICES CM 1978/C:47*, Int. Council. for the Explor. of the Sea, Copenhagen, 1978.
- Bacon, S., Decadal variability in the outflow from the Nordic Seas to the deep Atlantic Ocean, *Nature*, *394*, 871–874, 1998.
- Baringer, M. O., and J. F. Price, Momentum and energy balance of the Mediterranean outflow, *J. Phys. Oceanogr.*, *27*, 1678–1692, 1997.
- Dickson, B., J. Meincke, I. Vassie, J. Jungclaus, and S. Østerhus, Possible predictability in overflow from the Denmark Strait, *Nature*, *397*, 243–246, 1999.
- Dickson, R. R., and J. Brown, The production of North Atlantic Deep Water: Sources, rates, and pathways, *J. Geophys. Res.*, *99*, 12,319–12,341, 1994.
- Doney, S. C., and W. J. Jenkins, Ventilation of the deep western boundary current and abyssal western North Atlantic: estimates from tritium and ^3He distributions, *J. Phys. Oceanogr.*, *24*, 638–659, 1994.
- Fristedt, T., R. Hietala, and P. Lundberg, Stability properties of a barotropic surface-water jet observed in the Denmark Strait, *Tellus*, *51*, 979, 1999.
- Girton, J. B., Dynamics of transport and variability in the denmark strait overflow, Ph.D. thesis, University of Washington, Seattle, WA, 2001.
- Girton, J. B., and T. B. Sanford, Velocity profile

- measurements of the Denmark Strait Overflow, *Int. WOCE Newslett.*, 37, 28–30, 1999.
- Girton, J. B., T. B. Sanford, and R. H. Käse, Synoptic sections of the Denmark Strait overflow, *Geophys. Res. Lett.*, 28, 1619–1622, 2001.
- Griffiths, R. W., Inertial wave drag and the production of intense vortices by turbulent gravity currents, *Ocean Modeling*, 50, 9–12, 1983.
- Jiang, L., and R. W. Garwood, Jr., Three-dimensional simulations of overflows on continental slopes, *J. Phys. Oceanogr.*, 26, 1214–1233, 1996.
- Johnson, G. C., and T. B. Sanford, Secondary circulation in the Faroe Bank Channel outflow, *J. Phys. Oceanogr.*, 22, 927–933, 1992.
- Johnson, G. C., T. B. Sanford, and M. O’Neil-Baringer, Stress on the Mediterranean outflow plume I: Velocity and water property measurements, *J. Phys. Oceanogr.*, 24, 2072–2083, 1994.
- Käse, R. H., and A. Oschlies, Flow through Denmark Strait, *J. Geophys. Res.*, 105, 28,527–28,546, 2000.
- Killworth, P. D., Mixing on the Weddell Sea continental slope, *Deep-Sea Res.*, 24, 427–448, 1977.
- Krauss, W., and R. H. Käse, Eddy formation in the Denmark Strait overflow, *J. Geophys. Res.*, 103, 15,525–15,538, 1998.
- Livingston, H. D., J. H. Swift, and H. G. Ostlund, Artificial radionuclide tracer supply to the Denmark Strait overflow between 1972 and 1981, *J. Geophys. Res.*, 90, 6971–6982, 1985.
- MacCready, P., and P. B. Rhines, Slippery bottom boundary layers on a slope, *J. Phys. Oceanogr.*, 23, 5–22, 1993.
- Mauritzen, C., Production of dense overflow waters feeding the North Atlantic across the Greenland–Scotland Ridge. part 2: An inverse model, *Deep-Sea Res. I*, 43, 807–835, 1996.
- McCartney, M., K. Donohue, R. Curry, C. Mauritzen, and S. Bacon, Did the overflow from the Nordic Seas intensify in 1996–1997?, *Int. WOCE Newslett.*, 31, 3–7, 1998.
- Pedersen, F. B., Friction in a shallow two-layer flow in a rotating ocean, in *The physical oceanography of sea straits*, edited by L. Pratt, pp. 545–557, Kluwer Academic, The Netherlands, 1990.
- Price, J. F., and M. O. Baringer, Outflows and deep water production by marginal seas, *Progr. Oceanogr.*, 33, 161–200, 1994.
- Ross, C. K., Temperature–salinity characteristics of the “overflow” water in Denmark Strait during “OVERFLOW ’73”, *Rapp. P.-v. Réun. Cons. int. Explor. Mer.*, 185, 111–119, 1984.
- Rudels, B., P. Eriksson, H. Grönvall, R. Hietala, and J. Launiainen, Hydrographic observations in Denmark Strait in fall 1997, and their implications for the entrainment into the overflow plume, *Geophys. Res. Lett.*, 26, 1325–1328, 1999.
- Sanford, T. B., and R.-C. Lien, Turbulent properties in a homogeneous tidal bottom boundary layer, *J. Geophys. Res.*, 104, 1245–1257, 1999.
- Smethie, W. M., Jr., and R. A. Fine, Rates of North Atlantic Deep Water formation calculated from chlorofluorocarbon inventories, *Deep-Sea Res. I*, 48, 189, 2001.
- Smethie, W. M., Jr., and J. H. Swift, The tritium:krypton-85 age of Denmark Strait overflow water and Gibbs Fracture Zone water just south of Denmark Strait, *J. Geophys. Res.*, 94, 8265–8275, 1989.
- Smith, P. C., A streamtube model for bottom boundary currents in the ocean, *Deep-Sea Res.*, 22, 853–873, 1975.
- Smith, P. C., Baroclinic instability in the Denmark Strait Overflow, *J. Phys. Oceanogr.*, 6, 355–371, 1976.
- Stahr, F. R., and T. B. Sanford, Transport and bottom boundary layer observations of the North Atlantic Deep Western Boundary Current at the Blake Outer Ridge, *Deep-Sea Res. II*, 46, 205–243, 1999.
- Swaters, G. E., On the baroclinic instability of cold-core coupled density fronts on a sloping continental shelf, *J. Fluid Mech.*, 224, 361–382, 1991.
- Swift, J. H., The circulation of the Denmark Strait and Iceland–Scotland overflow waters in the

North Atlantic, *Deep-Sea Res.*, 31, 1339–1355,
1984.

This preprint was prepared with AGU's L^AT_EX macros
v5.01, with the extension package 'AGU++' by P. W. Daly,
version 1.6 from 1999/02/24.